

The two colors of MgB₂

V. Guritanu, A.B. Kuzmenko, and D. van der Marel

DPMC, University of Geneva, 24, Quai E.-Ansermet, 1211 Geneva 4, Switzerland

S.M. Kazakov, N.D. Zhigadlo, and J. Karpinski

Solid State Physics Laboratory, ETH 8093 Zurich, Switzerland

(Dated: December 17, 2018)

We present the anisotropic optical conductivity of MgB₂ between 0.1 and 3.7 eV at room temperature obtained on single crystals of different purity by the spectroscopic ellipsometry and reflectance measurements. The bare (unscreened) plasma frequency ω_p is almost isotropic and equal to 6.3 eV, which contrasts some earlier reports of a very small value of ω_p . The data suggests that the σ -bands are characterized by a stronger electron-phonon coupling λ_{tr} but smaller impurity scattering γ_{imp} , compared to the π -bands. The optical response along the boron planes is marked by an intense interband transition at 2.6 eV, due to which the reflectivity plasma edges along the a- and c-axes are shifted with respect to each other. As a result, the sample spectacularly changes color from a blueish-silver to the yellow as the polarization is rotated from the in-plane direction towards the c-axis. The optical spectra are in good agreement with the published *ab initio* calculations. The remaining discrepancies can be explained by the relative shift of σ -bands and π -bands by about 0.2 eV compared to the theoretical band structure, in agreement with the de Haas-van Alphen experiments. The widths of the Drude and the interband peaks are both very sensitive to the sample purity.

PACS numbers:

I. INTRODUCTION

The discovery of superconductivity in MgB₂¹ caused an excitement in the physics community not only due to an unprecedentedly high T_c (~ 40 K) for a 'conventional' electron-phonon superconductor, but also because it clearly shows the existence of two distinct gaps²; an intriguing phenomenon that, although addressed theoretically, had been never observed before. Magnesium diboride consists of graphite-like boron planes intercalated with Mg atoms. The metallic properties are determined by two distinct types of electronic bands: the strongly covalent almost 2D σ -bands formed by the hybridized sp_xp_y B orbitals and 3D π -bands made of p_z orbitals. The holes in the σ -bands are strongly coupled to the in-plane bond-stretching phonon modes, giving rise to a high electron-phonon coupling constant.³ A remarkable implication of such a strong conduction band disparity is a multigap superconductivity: a large gap value on σ -bands and a small one on π -bands. Notably, the community has enjoyed a rapid advance in understanding the electronic structure and superconducting scenario of MgB₂, in contrast to the lengthy siege of the high- T_c problem in the cuprates.

The early theoretical predictions of the electronic structure and the superconducting properties were soon confirmed by the isotope effect,^{4,5} angle-resolved photoemission,⁶ de Haas-van Alphen (dHvA),⁷ specific heat,^{8,9,10} tunneling measurements¹¹ and, recently, by the inelastic X-ray scattering.¹² Even though the far-infrared experiments^{13,14,15,16,17,18} have clearly shown the lowest of the superconducting gaps in agreement with the theory and other spectroscopic probes, the optical

measurements so far demonstrated a rather poor reproducibility and equally poor consistency with the theoretical electronic structure. The most controversial issue is value of the Drude plasma frequency ω_p . While the theory predicts a high value of ω_p of ≈ 7 eV, which corresponds to about 1 conducting electron per unit cell, a number of groups^{14,19,20,21,22,23} reported a much smaller value of about 1.5 - 2.5 eV, corresponding to 0.15 electrons per cell. In Ref.20, in addition to the narrow Drude peak, a broad continuum, which could contain the missing Drude spectral weight, was found below 1 eV. However, the existence of such a continuum was not reliably verified by other groups. Another inconsistency is related to the anisotropy of the plasma frequency. The calculations provide very close (within 5%) values of $\omega_{p,a}$ and $\omega_{p,c}$, which should be regarded, in fact, as a coincidence, because the plasma frequency of the carriers in the 2D σ -bands is strongly anisotropic. A study of the optical anisotropy of magnesium diboride was undertaken by Fudamoto and Lee²³ by the comparison of the reflectivity spectra measured on a mosaic of ab-oriented crystals and on a polycrystalline sample. They observed the in-plane reflectivity plasma edge at about 16000 cm⁻¹. The authors also suggested that an additional structure in the reflection of a polycrystal is due to the c-axis plasma edge at 22000 cm⁻¹. Thus the anisotropy ratio $\omega_{p,a}/\omega_{p,c} \approx 0.73$ was deduced, which is in contrast with the theoretical prediction.

The optically derived electron-phonon coupling constant λ_{tr} was also a subject of debate.^{19,22,24,25} Values of λ_{tr} ranging from 0.13¹⁹ to 1.5²² were reported. It was pointed out in Ref.25 that the determination of λ_{tr} relies strongly on the plasma frequency, which is not yet well established. One should keep in mind that different

values of the coupling constant for the σ - and π -bands are expected from the calculations³ and observed in the dHvA experiment.⁷

With a lack of large single crystals of MgB_2 , especially along the c -axis, the optical measurements were done on polycrystalline samples,^{18,20,23} disoriented^{22,26} or ab -oriented^{15,16,19} films as well as ab -oriented crystal mosaics.^{17,23} We believe that a large spread of the published optical results can be explained by (i) different purity levels of the samples used, (ii) experimental difficulties to extract the anisotropic complex conductivity from the standard measurements on such objects and (iii) a fast rate of the surface degradation in air.^{20,23}

In this work, we do optical experiments on individual freshly polished single crystals of different purity having no contact with the air. The real and imaginary parts of the in-plane and out-of-plane optical conductivities are derived from the reflectivity and ellipsometry measurements on the ab - and, for the first time, on the ac -oriented crystals. The measurements show a large (≈ 6.3 eV) and almost isotropic plasma frequency. We find different positions of the reflectivity plasma edges for the two light polarizations. However, such anisotropy is due to extra screening of charge carriers by an interband transition at 2.6 eV, optically active along the ab -plane, rather than the anisotropy of the bare plasma frequency itself. The anisotropic spectra are in satisfactory agreement with the first-principles calculations of the band structure and the electron-phonon interaction. We discuss the possible corrections to the electronic structure which follow from the optical results.

Finally, the presented data tell us what is the 'true' color (or rather, colors) of MgB_2 .

II. SAMPLES AND PREPARATION

High-quality single crystals of MgB_2 have been grown using a cubic anvil technique via the peritectic decomposition reaction of the MgNb_9 and Mg at temperature up to 2000°C under a pressure of 30 - 35 kbar. The details of the crystal growth and extensive characterization are given elsewhere.²⁷ The measurements were done on two samples, referenced below as S1 and S2. The samples were grown under slightly different conditions. For the sample S1 the purity of Mg was 99.8%, while a 4N-pure (99.98%) magnesium was used in the second case. The maximum temperature of crystal growth was higher for the sample S2 by about 80°C. The time at highest temperature was 10 minutes for the first sample and 30 minutes for the second one. The T_c of both samples is close to 38 K (see Fig.1), although sample S2 shows somewhat narrower transition and a larger field-cooled diamagnetic signal compared to the one of S1.

The dimensions ($a \times b \times c$) of the as-grown crystals were $0.7 \times 0.5 \times 0.27$ mm³ for S1 and $0.6 \times 0.5 \times 0.18$ mm³ for S2. We selected a thicker sample S1 to prepare the (ac) optical face, while sample S2 was used to measure

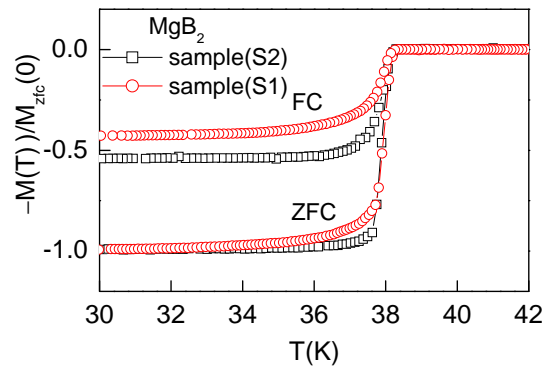


FIG. 1: Magnetization measurements of the superconducting transition of the two single crystals of MgB_2 used in this paper.

on the (ab) face. The faces were dry-polished using a 0.1 μm diamond abrasive, since the as-grown surfaces were not suitable for quantitative optical examination.

As it was noticed before,^{20,23} the exposed surface of MgB_2 deteriorates quickly, largely due to the air moisture. In order to avoid the contamination, the samples were kept in a flow of dry nitrogen during and after the polishing until the end of the measurements. With this precaution, the optical characteristics did not change noticeably during the experiment. On the other hand, switching off the flow immediately affected the optical signal as it is shown in the Appendix.

III. OPTICAL EXPERIMENT AND RESULTS

Optical properties of MgB_2 at room temperature were obtained using spectroscopic ellipsometry at 0.75 - 3.7 eV and the reflectivity measurements in the infrared range from 0.1 to 0.85 eV. In all experiments samples were mounted on the top of a sharp optically black cone and laser aligned.

The high-frequency spectra were collected using the Woollam VASE32 ellipsometer while the sample was kept in a flow of dry nitrogen. The in-plane $\epsilon_a(\omega) = \epsilon_{1,a}(\omega) + 4\pi i\sigma_{1,a}(\omega)/\omega$ and the c -axis $\epsilon_c(\omega) = \epsilon_{1,c}(\omega) + 4\pi i\sigma_{1,c}(\omega)/\omega$ components of the complex dielectric tensor were both extracted directly from the measurements on the ac -surface of the sample S1, using two orthogonal crystal orientations and three angles of incidence. For the sample S2, only the in-plane optical functions $\epsilon_{1,a}(\omega)$ and $\sigma_{1,a}(\omega)$ were derived from the measurement on the ab -plane, using the c -axis data from the sample S1 to correct for the admixture of the out-of-plane component. The details of the recovery of $\epsilon_a(\omega)$ and $\epsilon_c(\omega)$ from the ellipsometric output are given in the Appendix.

The reflectivity $R(\omega)$ was measured with a polarizer in the range 0.1 - 0.85 eV at a near-normal angle of incidence using a Fourier transform spectrometer Bruker 66v. The sample was inside a vacuum chamber of a cryostat. A gold layer was sputtered *in-situ* on the crystal

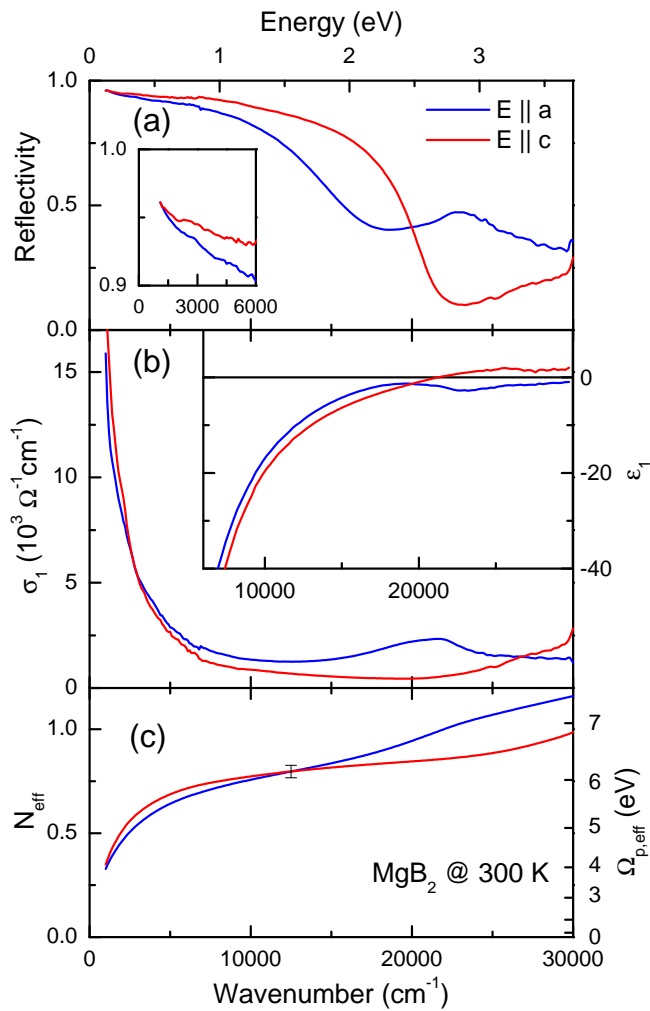


FIG. 2: Optical anisotropic spectra of the MgB_2 at 300 K derived from the ellipsometry and reflectivity measurements on the sample S1 as described in the text: the normal-incidence reflectivity $R(\omega)$ (a), optical conductivity $\sigma_1(\omega)$, the dielectric function $\epsilon_1(\omega)$ (b), the effective number of carriers $N_{\text{eff}}(\omega)$ and the effective plasma frequency $\Omega_{p,\text{eff}}(\omega)$ (c). The a-axis and the c-axis spectra are shown by the blue and red colors respectively.

surface to get a reference signal. We reconstructed the full reflectivity spectrum using the ellipsometrically determined dielectric functions in the optical range:

$$R_\nu(\omega) = \left| \frac{1 - \sqrt{\epsilon_\nu(\omega)}}{1 + \sqrt{\epsilon_\nu(\omega)}} \right|^2, (\nu = a, c). \quad (1)$$

The spectra from two regions were combined in order to obtain the complex dielectric function in the whole range. While $\epsilon(\omega)$ was measured directly above 0.75 eV, at low frequencies we applied a variational Kramers-Kronig (KK) constrained analysis of the data. In this method, described in Ref.28, one finds a KK-consistent dielectric function, which gives the best detailed match to the reflectivity $R(\omega)$ at low frequencies and both $\epsilon_1(\omega)$

and $\epsilon_2(\omega)$ at high frequencies simultaneously. This procedure reduces to a large extent the uncertainty due to extrapolations as compared to the usual KK transform.

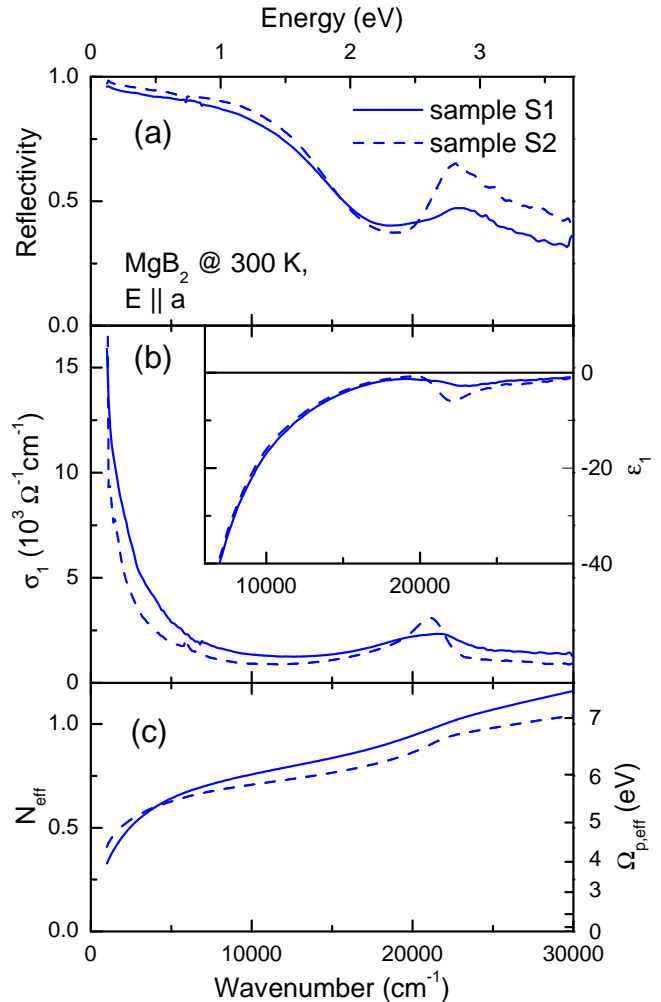


FIG. 3: Comparison of the in-plane optical spectra measured on different samples. The same types of spectra are presented as in Fig.2. The spectra of samples S1 and S2 are shown by the solid and dash lines, respectively. Sample S2 has presumably a smaller concentration of impurities than sample S1.

Figs.2a and 2b show the anisotropic reflectivity $R(\omega)$, optical conductivity $\sigma_1(\omega)$ and the dielectric function $\epsilon_1(\omega)$, measured on sample S1. Qualitatively, both in-plane and c-axis spectra exhibit a similar metallic behavior, characterized by a reflectivity plasma edge, a Drude peak in $\sigma_1(\omega)$ and negative $\epsilon_1(\omega)$. However, one can see a strong anisotropy. The in-plane reflectivity shows a broad plasma edge at about 2 eV. The dielectric function $\epsilon_{1,a}(\omega)$ almost reaches zero at the same frequency, but then it varies non-monotonically while remaining negative at least up to 3.7 eV. In contrast, the c-axis plasma edge is significantly sharper and is higher in energy by about 0.5-0.6 eV. Correspondingly, $\epsilon_{1,c}(\omega)$ behaves monotonically and crosses zero at $\omega_{p,c}^* \approx 2.6$ eV. These results agree with the previous findings of Fu-

damoto and Lee²³ who obtained a plasma edge at about 16000 cm^{-1} (2 eV) on a mosaic of ab-oriented crystals. Although no direct reflectivity measurements for $E \parallel c$ were reported so far, the same authors suggested²³ that the additional step-like structure at 22000 cm^{-1} (2.7 eV) in the reflectivity of polycrystals samples comes from the c-axis plasma edge. The present study fully confirms this assignment.

The in-plane optical conductivity $\sigma_{1,a}(\omega)$ shows an intense interband peak at $\sim 2.6 \text{ eV}$, which is totally absent in the $\sigma_{1,c}(\omega)$ (Fig.2b). Its origin will be discussed below. Since this peak is close to the screened plasma frequency, it broadens the plasma edge and shifts it to lower frequencies by providing an additional screening of the charge carriers. It is also responsible for a non-monotonic behavior of $\epsilon_{1,a}(\omega)$ at higher frequencies and even for a structure in $R_a(\omega)$ above 3 eV, which resembles a 'second' plasma edge.

Fig. 2c depicts the partial sum rule (effective number of carriers) function:

$$N_{\text{eff}}(\omega) = \frac{2mV_c}{\pi e^2} \int_0^\omega \sigma_1(\omega') d\omega', \quad (2)$$

where m is the free electron mass, $V_c = 28.9 \text{ \AA}^3$ is the unit cell volume, e is the electron charge, and the corresponding effective plasma frequency:

$$\Omega_{p,\text{eff}}(\omega) = \left[8 \int_0^\omega \sigma_1(\omega') d\omega' \right]^{1/2}. \quad (3)$$

Since the integration of $\sigma_1(\omega)$ has to start from zero frequency, while the optical data are taken down to 100 meV, one has to be vigilant about the error bars involved. Fortunately, the fact that the dielectric function obtained by the method used²⁸ satisfies the KK relations and describes both $\epsilon_1(\omega)$ and $\epsilon_2(\omega)$ at high frequencies poses fairly tight bounds (shown in Fig.2c) on the allowed values of N_{eff} . One can see that at the photon energy of 1.7 eV, which is high enough to comprise most of the intraband spectral weight, but below the interband peak at 2.6 eV, N_{eff} is about 0.8 for both polarizations, which corresponds to the plasma frequency of 6.3 eV. A more rigorous estimate which takes into account the broadening of the Drude peak, as described below, gives a very close value of ω_p . This is in contrast with the conclusion of Ref.23 about a strong anisotropy of the plasma frequency, based on the different positions of the reflectivity plasma edge for the two polarizations. The anisotropy of the reflectivity plasma edge is caused by extra screening due to the in-plane interband transition at 2.6 eV and not by the strong anisotropy of the unscreened plasma frequency.

It is interesting to compare the in-plane optical properties of the two samples (S1 and S2), which were prepared under different conditions and have presumably slightly different impurity levels (see Fig.3). One can see that the two most prominent features of the optical conductivity - the Drude peak and the 2.6 eV interband peak - are

significantly sharper in the sample S2. As a result, the reflectivity plasma edge is also sharper and the 'double-plasmon' structure in $R_a(\omega)$ is more pronounced than in sample S1. One should keep in mind that the sample S2 was prepared from a slightly more pure magnesium, and it shows a sharper superconducting transition (Fig.1). This tells that even a small impurity level (about 0.2% in this case) affects significantly optical and transport properties.

The close values of $\epsilon_{1,a}(\omega)$ for the two samples suggest that their in-plane plasma frequencies are similar, although the N_{eff} is slightly higher for sample S1, which could be related to a stronger broadening of the interband peaks.

IV. DISCUSSION

A. Extended Drude analysis

The extended Drude model has been commonly used to analyze interactions in electronic systems. In this formalism, the frequency dependent scattering rate $1/\tau(\omega)$ and effective mass $m^*(\omega)/m$ are derived from the measured complex dielectric function:

$$\frac{1}{\tau(\omega)} = -\frac{\omega_p^2}{\omega} \text{Im} \left(\frac{1}{\epsilon(\omega) - \tilde{\epsilon}_\infty} \right), \quad (4)$$

$$\frac{m^*(\omega)}{m} = -\frac{\omega_p^2}{\omega^2} \text{Re} \left(\frac{1}{\epsilon(\omega) - \tilde{\epsilon}_\infty} \right). \quad (5)$$

The only parameters of this conversion are the total Drude plasma frequency ω_p and the high-frequency dielectric constant $\tilde{\epsilon}_\infty$, due to all contributions other than the conductivity electrons. Both $1/\tau(\omega)$ and $m^*(\omega)/m$ have direct microscopic interpretation in the context of the electron-phonon interaction. One should keep in mind, however, that the model assumes that only one type of carriers contributes to the Drude response. In the case of MgB₂, which has two distinct systems of bands (σ and π), the scattering rate and the effective mass obtained by Eqs.(4) and (5) should be regarded as an averaged value of contributions from each band. Fig.4 (symbols) shows $1/\tau(\omega)$ and $m^*(\omega)/m$ for the in-plane and the c-axis directions, measured on the sample S1. We took the values $\omega_{p,a} = 6.28 \text{ eV}$, $\omega_{p,c} = 6.35 \text{ eV}$, $\tilde{\epsilon}_{\infty,a} = 11.9$, $\tilde{\epsilon}_{\infty,c} = 4.77$, which are suggested by the data fitting in Section IV C (see Table I). The value of $\tilde{\epsilon}_\infty$ here is given by the sum of ϵ_∞ in the Table I and the oscillator strengths S_i of the Lorentz oscillators. The solid curves in Fig.4 were calculated using the results of the fit described in Section IV C.

One can see that the scattering rate and the mass renormalization are larger for the in-plane direction. It is worth mentioning that the σ -bands with a cylinder-like Fermi surface must have a small electromagnetic response along the c-axis, while the π -bands are expected to have comparable contributions in both directions. The present

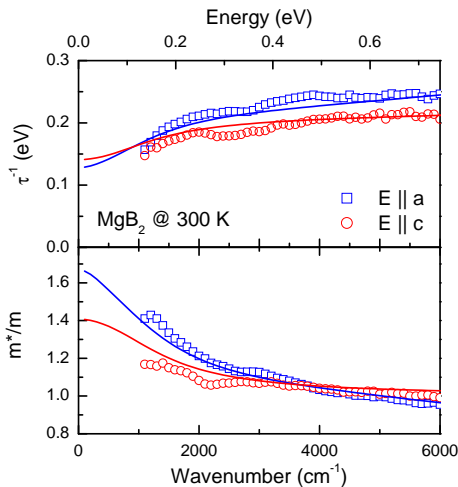


FIG. 4: Extended Drude analysis of the optical conductivity of MgB₂ (sample S1) at 300 K along the in-plane and the c-axis directions. The symbols are the data, the solid curves show the two-component fit as described in the Section IV C.

result thus suggests that the electron-phonon coupling is stronger in the σ -bands. This is in agreement with the first-principle calculations of Kong *et al.*,³ who found that the total strength of the electron-phonon interaction is dominated by the coupling of the σ -holes to the bond-stretching optical phonons. A quantitative analysis of the electron-phonon interaction must take into account the multi-band electronic structure.

B. Comparison with *ab initio* calculations

A deeper insight can be attained by the comparison of the optical data with the existing first-principle calculations of the band structure and electron-phonon interaction. One can compute the dielectric function, assuming that the intraband optical conductivity is formed by the additive contributions of carriers in the σ - and the π -bands. The two bands are characterized by different electron-phonon (Eliashberg) transport functions $\alpha_{tr}^2 F(\omega)$ and impurity scattering rates γ_{imp} . Intraband optical response can be calculated using finite-temperature memory-function formalism for electron-boson interaction.²⁹ The total conductivity is a sum of the intraband, interband (ϵ^{IB}) and core-electron (ϵ_{∞}) responses:

$$\epsilon_{\nu}(\omega) = \sum_{\beta=\sigma,\pi} \frac{\omega_{p,\nu\beta}^2}{-\omega[\omega + iM_{\beta}(\omega, T)]} + \epsilon_{\nu}^{IB}(\omega) + \epsilon_{\nu\infty} \quad (6)$$

$(\nu = a, c).$

The contribution of each of the two bands is determined by its respective anisotropic plasma frequency ($\omega_{p,a}$, $\omega_{p,c}$)

and the memory function²⁹:

$$M_{\beta}(\omega, T) = \gamma_{\beta imp} - 2i \int_0^{\infty} d\Omega \alpha_{tr}^2 F_{\beta}(\Omega) K\left(\frac{\omega}{2\pi T}, \frac{\Omega}{2\pi T}\right), \quad (7)$$

where

$$K(x, y) = \frac{i}{y} + \frac{y-x}{x} [\psi(1-ix+iy) - \psi(1+iy)] + \frac{y+x}{x} [\psi(1-ix-iy) - \psi(1-iy)],$$

and $\psi(x)$ is a digamma function.

All the ingredients to compute $\epsilon(\omega)$, except the impurity scattering rates $\gamma_{\sigma imp}$ and $\gamma_{\pi imp}$, which depend on the level and the nature of the impurities (substitutions, vacancies, dislocations etc.), are provided by the *ab initio* LDA calculations.

The spectra of the interband optical conductivity $\sigma_1^{IB}(\omega)$ obtained by different groups using the LMTO,^{30,31} full-potential LAPW³² and time-dependent DFT³³ methods, although showing some differences, are close to each other. In particular, we took the interband conductivity spectra, presented in Ref.20 (Fig.5) on the base of the full-potential LAPW method,³² and computed the corresponding dielectric function $\epsilon_1^{IB}(\omega)$ by the KK transformation. The plasma frequencies reported by different groups^{30,31,32} are also close to each other. We used the values $\omega_{p,a\sigma} = 4.14$ eV, $\omega_{p,a\pi} = 5.89$ eV, $\omega_{p,c\sigma} = 0.68$ eV and $\omega_{p,c\pi} = 6.85$ eV.^{21,32}

The *ab initio* calculated electron-phonon interaction functions were presented in Ref.3. We used effective interaction functions for the two bands $\alpha_{tr}^2 F_{\sigma}(\omega) \equiv \alpha_{tr}^2 F_{\sigma\sigma}(\omega) + \alpha_{tr}^2 F_{\sigma\pi}(\omega)$ and $\alpha_{tr}^2 F_{\pi}(\omega) \equiv \alpha_{tr}^2 F_{\pi\pi}(\omega) + \alpha_{tr}^2 F_{\pi\sigma}(\omega)$ from the Refs.3,10,34. The electron-phonon coupling constant $\lambda_{tr} = 2 \int_0^{\infty} d\Omega \alpha_{tr}^2 F(\Omega)/\Omega$ is calculated to be about 1.1 for the σ -bands and 0.55 for the π -bands.

The calculated optical spectra are presented in Fig.5. Here the scattering rates $\gamma_{\sigma imp} = 12.4$ meV and $\gamma_{\pi imp} = 85.6$ meV were taken; this choice is substantiated by the data fitting in the next Section. Comparing Figs.2 and 5, one can notice a remarkable overall agreement and even a reasonable quantitative match.

We begin with the interband transitions. Both theoretical and experimental interband optical conductivities show a very strong anisotropy. Notably, the theory predicts no sizeable optical intensity along the c-axis of the interband transitions below 4 eV, whereas there are two low-lying peaks at 0.35 eV and 2.4 eV for polarization parallel to the boron planes (see the blue dashed curve in Fig.5b). The 2.4 eV peak is due to a transition from the σ -band to the π -band close to the M-point, where a van Hove singularity strongly enhances the density of states.³² The peak at 0.35 eV corresponds to the transition between two close σ -bands. The σ carriers are localized within the boron planes, which explains why these two transitions are optically very weak along the c-axis.

Obviously, a strong peak in the experimental spectrum along the a-axis at 2.6 eV matches the theoretical peak

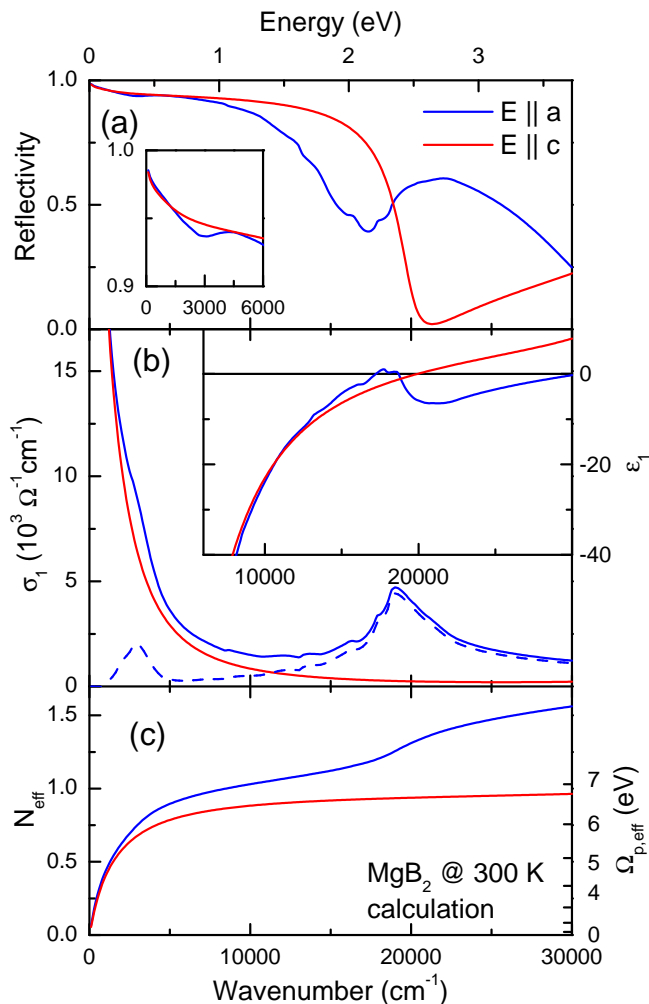


FIG. 5: Anisotropic optical spectra of MgB₂ at 300 K, calculated using the results of the published first-principle studies^{3,32} as described in the text. The same types of spectra are shown as in Fig.2. Additionally, the interband contribution along the a-axis is presented in (b) as a dashed blue line. The interband conductivity along the c-axis is negligible in the shown energy range.

at 2.4 eV. The discrepancy in the peak position suggests that the separation between σ -band and π -band is about 0.2 eV bigger than predicted by the theory. It is remarkable,³⁵ that the same shift brings the results of the dHvA experiments⁷ in MgB₂ close to theoretical predictions.^{35,36}

According to the calculation, the $\sigma \rightarrow \sigma$ transition at 0.35 eV should manifest itself as a noticeable dip in the reflectivity spectrum (see inset in Fig.5a). Such a dip is not observed in the experimental spectra (Fig.2a). This peak may thus be shifted to even lower frequencies or heavily overdamped. The first possibility is consistent with a shift of the σ -bands with respect to the Fermi energy compared to the calculation, as proposed in Ref.35. The broadening can be caused by the interaction with the conduction electrons, since the energy of this transition

is within the width of the Drude peak.

A very intense sharp peak in the out-of-plane conductivity $\sigma_{1,c}(\omega)$ is expected around 5 eV.^{20,30,33} This excitation was closely studied in Ref.33 by the time-dependent DFT method. In the band picture, it comes from a transition between almost parallel bands. From the real-space point of view, this mode involves charge fluctuations between B and Mg sheets, dynamically screened by the intraband transitions.³³ As a consequence, a sharp plasma mode at 2.5 eV should emerge. Although 5 eV is beyond our experimental range, there is a sizeable increase of $\sigma_{1,c}(\omega)$ above 3 eV, which can be a low-energy tail of this mode. The c-axis plasmon is at 2.6 eV, which is only slightly higher than the calculated value (~ 2.5 eV). This is in agreement with the inelastic X-ray scattering experiment.¹²

The shape and the width of the Drude peak agree well with the experiment, which suggests that phonons and impurities are the main factors of electron scattering. The integrated spectral weight $N_{\text{eff}}(\omega)$ grows faster according to the calculations, especially for the in plane response. This indicates that the theory overestimates the value of the plasma frequency.

C. Two-band fitting of the spectra

The overall good agreement between the experimental and calculated data allows us to use the chosen model to fit the spectra, treating the plasma frequencies and scattering rates as adjustable parameters. We could achieve a satisfactory least-square fit of reflectivity $R(\omega)$ in the mid-infrared and $\epsilon_1(\omega)$ and $\sigma_1(\omega)$ at higher frequencies using formulas (6) and (7) as it is shown in Fig.6. The corresponding parameter values are given in Table I.

It turns out that leaving all four plasma frequencies adjustable makes the fitting procedure under-determined. Therefore, assuming the 2D nature of the σ -band, we fixed the plasma frequencies of the σ -band to the values given by *ab initio* calculations, and left only the total in-plane and c-axis plasma frequencies $\omega_{p,tot}^2 = \omega_{p,\sigma}^2 + \omega_{p,\pi}^2$ adjustable. Another assumption was that the *ab initio* calculations^{3,10,34} correctly describe the electron-phonon functions $\alpha_{\nu}^2 F_{\sigma,\pi}(\omega)$.

We modelled the interband conductivities by Lorentz oscillators ($\nu = a, c$):

$$\epsilon_{\nu}^{IB}(\omega) = \sum_i \frac{S_{\nu i} \omega_{\nu i}^2}{\omega_{\nu i}^2 - \omega^2 - \gamma_{\nu i} \omega}. \quad (8)$$

with adjustable frequency $\omega_{\nu i}$, oscillator strength $S_{\nu i}$ and width $\gamma_{\nu i}$. Keeping in mind the two interband peaks below 3 eV predicted by the theory, we put two Lorentzians to model $\epsilon_{\nu}^{IB}(\omega)$. Only one oscillator term above 3 eV was taken for $\epsilon_c^{IB}(\omega)$.

One can see that the bare plasma frequencies $\omega_{p,\sigma}$ and $\omega_{p,\pi}$ are almost the same and equal to 6.3 eV, which confirms our previous estimate based on the partial sum

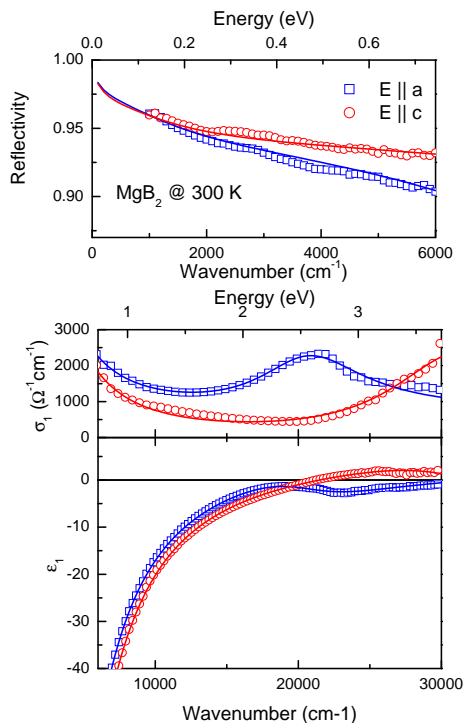


FIG. 6: Experimental data (symbols) and the multi-band fit (solid lines) of the reflectivity (a) and the dielectric function (b) along the a-axis (blue) and the c-axis (red).

rule (Fig.2c). This value is much higher compared to previous reports^{14,19,20,21,22,23} of 1.5-2.5 eV. Thus, the discrepancy with the theoretical value of 7 eV is likely to be much less than it was thought before. However, the current mismatch is not negligible since it results in about 20-25% deviation of the Drude spectral weight. It is worth to mention that the extremal orbit areas in the de Haas-van Alphen experiment⁷ on both σ and π Fermi surfaces are also somewhat smaller than predicted by theory.^{35,36} It was pointed out³⁵ that the discrepancy can be removed by a shift of the σ -bands downward by about 115 meV and the π -bands upward by 125 meV. This is in perfect agreement with our observation of the mismatch of 0.2 eV in the position of the 2.6 eV peak, as it is mentioned before. This also qualitatively explains the smaller value of the plasma frequency.

The impurity scattering rate in the π -band $\gamma_{\pi imp}$ is about 85 meV. Since the π -electrons have rather strong optical spectral weight and a modest electron-phonon interaction, the absolute values of both $R_a(\omega)$ and $R_c(\omega)$ are quite sensitive to this parameter. In contrast, the value of $\gamma_{\sigma imp}$ does not significantly affect the spectra and cannot be accurately determined from the fit, because a large electron-phonon interaction in the σ -band dominates the total scattering above 100 meV at 300 K. However, $\gamma_{\sigma imp}$ influences drastically the shape of the temperature-dependent in-plane DC resistivity $\rho_a(T) = 1/\sigma_{1,a}(\omega \rightarrow 0, T)$ curves, most notably the value of $\rho(300K)/\rho(40K)$ (RRR), as can be seen from Fig.7.

TABLE I: Model parameters which give the best match to the measured optical spectra of MgB₂ at 300 K and the ratio $\rho_a(300K)/\rho_a(40K)$ from Ref.37, as described in the text. Parameters, marked by *, were fixed to the values given by the band calculations.

Parameter	ab-plane	c-axis
$\omega_{p,\sigma}$	4.14* eV	0.68* eV
$\omega_{p,\pi}$	4.72 eV	6.31 eV
$\omega_{p,tot}$	6.28 eV	6.35 eV
$\gamma_{\sigma imp}$	12.4 meV	
$\gamma_{\pi imp}$	85.6 meV	
ω_1	2.60 eV	3.92 eV
S_1	1.79	1.7
γ_1	1.11 eV	1.51 eV
ω_2	8.57 eV	-
S_2	6.81	-
γ_2	100.2 eV	-
ϵ_∞	3.31	3.07

A measurement³⁷ on a crystal grown in the same group under similar condition, showed $RRR \approx 5$ along the a-axis. Therefore we have chosen of $\gamma_{\sigma imp} = 12.4$ meV, which gives the same resistivity ratio (see Fig.7). The assumption $\gamma_{\sigma imp} = \gamma_{\pi imp}$ gives RRR less than two, which strongly suggests that $\gamma_{\sigma imp}$ is actually several times smaller than $\gamma_{\pi imp}$. This agrees with the Raman study³⁸ on single crystals, where a relation $\gamma_{\pi imp}/\gamma_{\sigma imp} = 6 - 9$ was found, although the absolute values of the scattering rates are smaller than in our case.

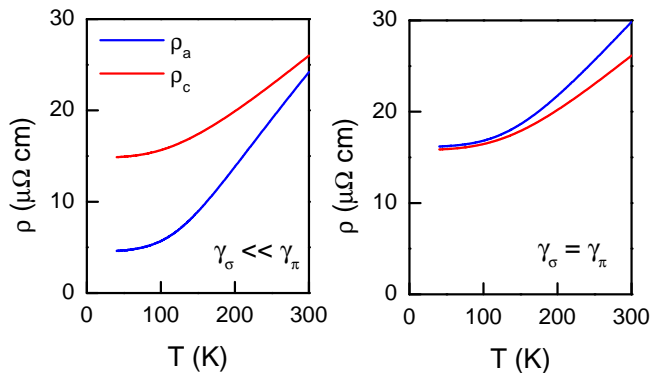


FIG. 7: Temperature-dependent resistivity curves along the a-axis (blue) and c-axis (red), calculated using the results of the fit of the optical data for $\gamma_{\pi imp} = 85.6$ meV and different values of the scattering rate in the σ -band: $\gamma_{\sigma imp} = 12.4$ meV $\ll \gamma_{\pi imp}$ (left) and $\gamma_{\sigma imp} = \gamma_{\pi imp}$ (right).

A disparity between the impurity scattering rates in the two bands and a small interband $\sigma \leftrightarrow \pi$ scattering were proposed in Ref.21 to explain the surprisingly small dependence of T_c on the impurity level, not expected for a two-band superconductor. Microscopically, this can be explained by the fact that the electronic wavefunctions in σ -bands are confined to the boron planes and not efficiently scattered by the magnesium vacancies and substitutions. On the other hand, the same defects strongly

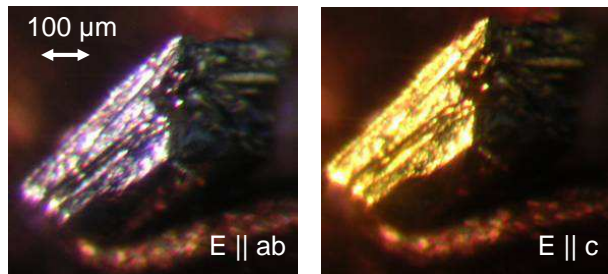


FIG. 8: Two images of the same sample (ac -plane) made in a polarized light: $E \parallel ab$ (left) and $E \parallel c$ (right). The sample looks golden for $E \parallel c$, due to a sharp reflectivity plasma edge at around 2.5 eV, while the plasma edge is smeared for $E \parallel ab$ by a strong $\sigma \rightarrow \pi$ interband transition at 2.6 eV.

scatter the electron states in the 3D π -bands. Our results support this conjecture.

The first Lorentz term for the a -axis at 2.6 eV clearly corresponds to the discussed already interband transition. However, the second oscillator is extremely broad and it cannot be matched with a predicted interband peak at 0.35 eV. This probably means this relatively weak peak is shifted and/or broadened so much that it cannot be identified in the optical spectrum. The second Lorentz term may thus describe the background formed by the tails of several broadened interband peaks.

D. The color of the magnesium diboride

Finally we address a practical question: what is the color of MgB_2 ? The characterizations given in the literature varied significantly, ranging from the 'golden' and 'tan' to 'silver-metallic', 'black' and even 'blue'. Lee³⁹ has noticed that, depending on the polarization, "...the fresh surface of as-grown crystals in the ab -plane changes the color from silver to dark gray. In contrast, for the ac -plane of the crystals a beautiful change of color from golden-yellow to blue can be seen." Fig.8 shows the two images of the unpolished ac -plane of the sample S1 for different polarizations of the incident white light. One can see that the sample spectacularly changes color from a blueish-silver for $E \parallel ab$ to the yellow for $E \parallel c$. The explanation comes naturally from the reflectivity curves shown in Fig.2a. For the c -axis polarization, it is a sharp plasma edge at about 2.5 eV, the same as of gold, which makes the sample yellow. For the ab -plane polarization, the plasma edge is smeared due to the strong interband transition at 2.6 eV. As a result, the reflectivity spectrum in the visible range (1.8 - 3.1 eV) is relatively flat with a maximum (stronger in sample S2) at ~ 2.8 eV which makes the color blue-silver.

Knowing the anisotropic spectra, we can predict the reflectivity shape of MgB_2 in the polycrystalline form. If the light wavelength λ is much larger than a typical grain size l , one can apply the effective-medium approximation (EMA) as prescribed in Ref.40. In the short-

wavelength limit $\lambda \ll l$, it is more adequate to average directly the reflectivities along the two axes, as it was done in Ref.23. In Fig.9 both calculated curves $R_{EMA}(\omega)$ (for sphere-like and plate-like crystallites) and $R_{av}(\omega) = (2/3)R_{ab}(\omega) + (1/3)R_c(\omega)$ are shown, together with the spectrum on a polycrystal from our previous study.²⁰ Notably, $R_{EMA}(\omega)$ and $R_{av}(\omega)$ are close to each other and their overall shape in the visible range matches well the measured spectrum. The latter shows only a weak step-like feature near 2.5 eV, coming from the c -axis contribution,²³ which explains why the polycrystalline samples have typically black, or slightly tan, color. The absolute value of the experimental reflectivity from Ref.20 is by 10-20% lower than the calculated one, which is likely caused by an overdamping of the π -bands due to a much higher impurity level (presumably MgO) of the sample used.

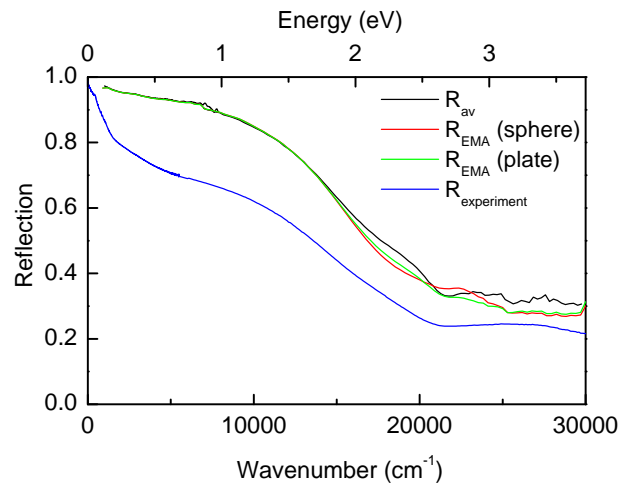


FIG. 9: Reflectivity spectra of polycrystalline MgB_2 at 300 K. The spectra, calculated using the effective-medium approximation (spherical or plate-like crystallites) and the direct reflectivity averaging, are compared with experimental spectrum from Ref.20.

V. CONCLUSIONS

We investigated anisotropic optical properties of MgB_2 single crystals of different purity at room temperature in the energy range 0.1 - 3.7 eV and compared them with the existing first principle calculations of the electronic structure and electron-phonon coupling. The analysis of the anisotropy allowed us to distinguish properties of the σ - and π -bands.

The total bare plasma frequencies along the in-plane and c -axis directions are almost the same and equal to 6.3 eV, which is much higher than the previously reported values. However, it is still smaller than the theoretical value of about 7 eV.

The shape of the Drude peak is well described by the electron scattering on phonons and impurities. The data

suggest that the impurity scattering in the π -bands is several times larger than in the σ -bands in agreement with a proposal of Ref.21, aimed to explain a surprisingly small dependence of the critical temperature on the sample purity. The electron-phonon interaction is stronger in the σ -bands, in agreement with the theory³ and de Haas-van Alphen experiments.⁷

The in-plane optical conductivity clearly shows an intense peak at 2.6 eV, which corresponds to a transition from the σ - to the π -band. It is higher by about 0.2 eV than the theoretical value. An interband peak due to the transitions between two close σ -bands, expected to be at 0.35 eV, was not seen in the experiments which can be explained by an overdamping or a shift towards lower frequencies relative to the theoretical calculations.

The width of the Drude peak and the interband $\sigma \rightarrow \pi$ peak at 2.6 eV are very sensitive to the sample purity. This can partially explain the spread of the results of previous optical studies.

The two quantitative mismatches between the experiment and the theory, namely (i) a smaller plasma frequency, (ii) a higher by 0.2 eV energy of the 2.6 eV $\sigma \rightarrow \pi$ transition, tell us that the σ -bands are probably shifted down and π -bands are shifted up compared to the calculations, so that their relative shift is about 0.2 eV. Notably, the same conclusion was derived in Ref.35 from the analysis of the dHvA measurements.⁷

The positions of the reflectivity plasma edges for two polarizations are very different (~ 2 eV for a-axis and ~ 2.5 eV for the c-axis). This is caused by an additional screening of the intraband carriers by the interband transition at 2.6 eV, but not due to different ab-plane and c-axis bare plasma frequencies. As a result, the color of the sample depends on the polarization of the light: it is blueish-silver for $E \parallel a$ and yellow for $E \parallel c$.

This work was supported by the Swiss National Science Foundation through the National Center of Competence in Research Materials with Novel Electronic Properties - MaNEP. We are grateful to O.V. Dolgov, J. Kortus and I.I. Mazin for fruitful discussions and kindly sharing their computational data. We thank R. Tediosi for making a picture of the sample.

Appendix. Determination of $\epsilon_a(\omega)$ and $\epsilon_c(\omega)$ from ellipsometry

The general geometry of the ellipsometric experiment in the configuration 'fixed analyzer (at 45°) - sample - rotating analyzer' is shown on Fig.10a. The axes x , y and z are assumed to be along the principal axes of the dielectric tensor of the sample. Ellipsometry provides two parameters ψ and Δ , related to the ratio of reflection coefficients for the p - and s -polarized light:

$$\rho = r_p/r_s = \tan \psi \exp(i\Delta). \quad (9)$$

r_p and r_s are given by the Fresnel formulas:

$$r_p = \frac{\sqrt{1 - \epsilon_z^{-1} \sin^2 \theta} - \sqrt{\epsilon_x} \cos \theta}{\sqrt{1 - \epsilon_z^{-1} \sin^2 \theta} + \sqrt{\epsilon_x} \cos \theta}, \quad (10)$$

$$r_s = \frac{\cos \theta - \sqrt{\epsilon_y - \sin^2 \theta}}{\cos \theta + \sqrt{\epsilon_y - \sin^2 \theta}}, \quad (11)$$

where $\epsilon_\nu = \epsilon_{1\nu} + i\epsilon_{2\nu}$ ($\nu = x, y, z$) are the components of the complex dielectric tensor. In the case of optically uniaxial MgB_2 ($\epsilon_a = \epsilon_b \neq \epsilon_c$) three different orientations (xyz) are possible: (aac) , (aca) and (caa) (see Fig.10b).

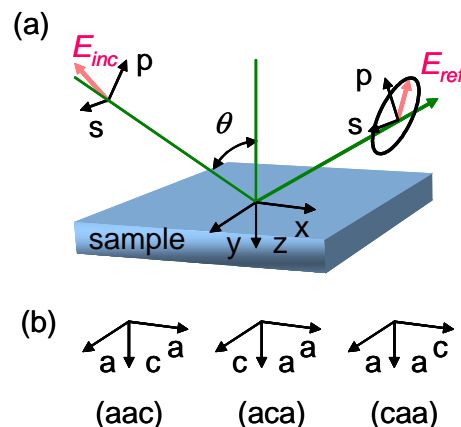


FIG. 10: (a) The general configuration of ellipsometric experiment; (b) three specific sample orientations used in this paper.

On the sample S1 we did ellipsometry in the orientations (caa) and (aca) . This yields four independent quantities ψ_{aca} , Δ_{aca} , ψ_{caa} and Δ_{caa} at every photon energy and every chosen angle of incidence. Since each of these functions depend on the four values $\epsilon_{1,a}$, $\epsilon_{2,a}$, $\epsilon_{1,c}$ and $\epsilon_{2,c}$, the latter ones can be obtained by the numerical inversion of the four Fresnel equations. This procedure, when applied to three different angles of incidence (60° , 70° and 80°), gave close results. In order to improve the accuracy of the output, we determined by the least square fitting the values of $\epsilon_{1,a}$, $\epsilon_{2,a}$, $\epsilon_{1,c}$ and $\epsilon_{2,c}$ that render the best match to the measured ellipsometric parameters at

all mentioned angles of incidence simultaneously. The experimental and fitting curves for the sample S1 for the orientations (*aca*) and (*caa*) are shown in Figs.11a and 11b respectively.

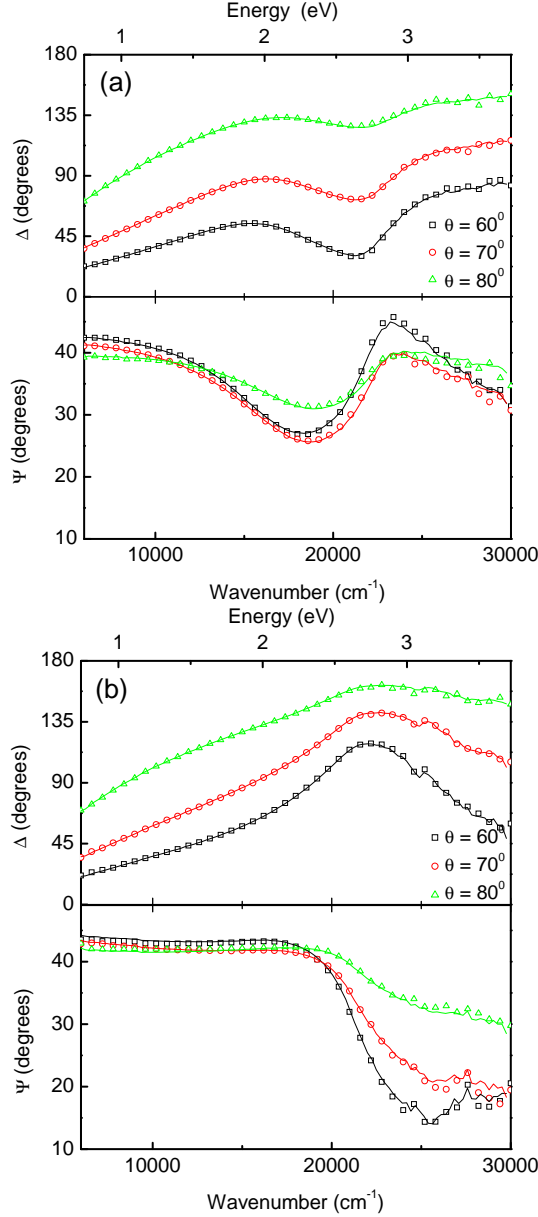


FIG. 11: Ellipsometric spectra ψ and Δ for three angles of incidence (60° , 70° , and 80°) in the orientations (*aca*)(a) (*caa*)(b) and (see Fig.10b), measured on sample S1. Symbols are the measurement results, the solid line correspond to the fit as described in the text.

The second experiment was done on the sample S2 in the orientation (*aac*). The corresponding spectra of ψ_{aac} and Δ_{aac} for the same three angles of incidence are shown in Fig.12 (as solid symbols). These data, taken alone, are not sufficient to extract both ϵ_a and ϵ_c independently. Since ψ_{aac} and Δ_{aac} are not very sensitive to the value of ϵ_c except close to the screened plasma frequency (ac-

cording to Aspnes approximation),⁴¹ we extracted $\epsilon_a(\omega)$, assuming that $\epsilon_c(\omega)$ is the same as the sample S1. One should realize that this introduces some uncertainty, because the samples S1 and S2 might have somewhat different c-axis dielectric functions. This uncertainty is negligible below 2 eV, but somewhat enhanced close to the c-axis plasmon at 2.6 eV. The best fit of ψ and Δ is given by the solid lines in Fig.12.

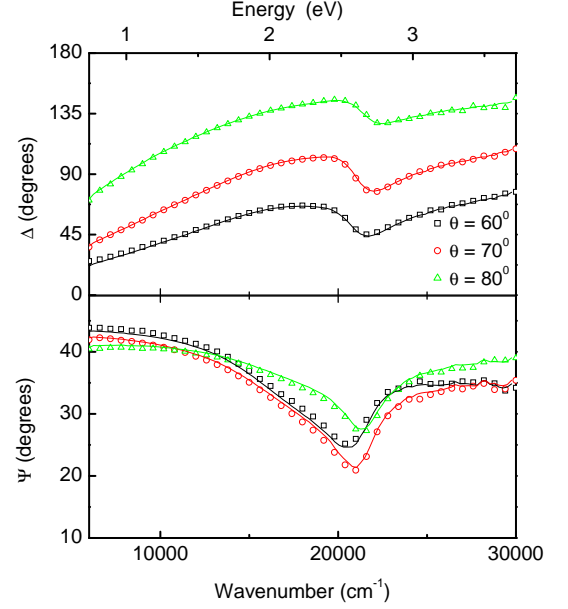


FIG. 12: Ellipsometric spectra ψ and Δ for three angles of incidence (60° , 70° , and 80°) in the orientation (*aac*) (see Fig.10b), measured on sample S2. Symbols are the measurement results, the solid line correspond to the fit as described in the text.

Fig.13 shows how quickly the ellipsometric parameters change when a surface is exposed to the air, due to the formation of a contamination layer.

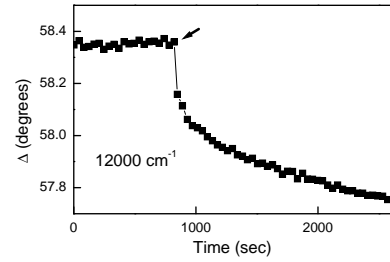


FIG. 13: The effect of the exposure to the air on the optical properties of MgB_2 . The time dependence of ellipsometric parameter Δ at 12000 cm^{-1} is shown (sample S1, geometry (*caa*), angle of incidence 70°). Initially the sample was kept in a flow of dry nitrogen, which was switched off at the moment designated by the arrow.

-
- ¹ J. Nagamatsu, N. Nakagawa, T. Muranaka, Y. Zenitani, and J. Akimitsu, *Nature* **410**, 63 (2001).
- ² I. I. Mazin and V.P. Antropov, *Physica C* **385**, 49 (2003).
- ³ Y. Kong, O.V. Dolgov, O. Jepsen, and O.K. Andersen, *Phys. Rev. B* **64**, 020501(R) (2001).
- ⁴ S. L. Bud'ko, G. Lapertot, C. Petrovic, C.E. Cunningham, N. Anderson, and P.C. Canfield, *Phys. Rev. Lett.* **86**, 1877 (2001).
- ⁵ D.G. Hinks, H. Claus, and J.D. Jorgensen, *Nature* **411**, 6836 (2001).
- ⁶ H. Uchiyama, K.M. Shen, S. Lee, A. Damascelli, D.H. Lu, D.L. Feng, Z.-X. Shen, and S. Tajima, *Phys. Rev. Lett.* **88**, 157002 (2002).
- ⁷ E.A. Yelland, J.R. Cooper, A. Carrington, N.E. Hussey, P.J. Meeson, S. Lee, A. Yamamoto, and S. Tajima, *Phys. Rev. Lett.* **88**, 217002 (2002).
- ⁸ Y. Wang, F. Bouquet, I. Sheikin, P. Toulemonde, B. Revaz, M. Eisterer, H.W. Weber, J. Hinderer, and A. Junod, *J. Phys.: Condens. Matter* **15**, 883 (2003).
- ⁹ F. Bouquet, Y. Wang, I. Sheikin, T. Plackowski, A. Junod, S. Lee, and S. Tajima, *Phys. Rev. Lett.* **89**, 257001 (2002).
- ¹⁰ A. A. Golubov, J. Kortus, O. V. Dolgov, O. Jepsen, Y. Kong, O. K. Andersen, B. J. Gibson, K. Ahn and R. K. Kremer *J. Phys.: Condens. Matter* **14**, 1353-1360 (2002).
- ¹¹ M. R. Eskildsen, M. Kugler, S. Tanaka, J. Jun, S. M. Kazakov, J. Karpinski, and O. Fischer, *Phys. Rev. Lett.* **89**, 187003 (2002).
- ¹² S. Galambosi, J.A. Soininen, A. Mattila, S. Huotari, S. Manninen, Gy. Vanko, N. D. Zhigadlo, J. Karpinski, and K. Hamalainen, *Phys. Rev. B* **71**, 060504(R) (2005).
- ¹³ B. Gorshunov, C.A. Kuntscher, P. Haas, M. Dressel, F.P. Mena, A.B. Kuzmenko, D. van der Marel, T. Muranaka, and J. Akimitsu, *Eur. Phys. J. B* **21**, 159 (2001).
- ¹⁴ R.A. Kaindl, M.A. Carnahan, J. Orenstein, D.S. Chemla, H.M. Christen, Hong-Ying Zhai, M. Paranthaman, and D.H. Lowndes, *Phys. Rev. Lett.* **88**, 027003 (2002).
- ¹⁵ A. Pimenov, A. Loidl, and S.I. Krasnosvobodtsev, *Phys. Rev. B* **65**, 172502 (2002).
- ¹⁶ J.H. Jung, K.W. Kim, H.J. Lee, M.W. Kim, T.W. Noh, W.N. Kang, Hyeong-Jin Kim, Eun-Mi Choi, C.U. Jung, and Sung-Ik Lee, *Phys. Rev. B* **65**, 052413 (2002).
- ¹⁷ A. Perucchi, L. Degiorgi, J. Jun, M. Angst, and J. Karpinski, *Phys. Rev. Lett.* **89** 097001 (2002).
- ¹⁸ M. Ortolani, D. Di Castro, P. Postorino, I. Pallecchi, M. Monni, M. Putti, and P. Dore, *Phys. Rev. B* **71**, 172508 (2005).
- ¹⁹ J.J. Tu, G.L. Carr, V. Perebeinos, C.C. Homes, M. Strongin, P.B. Allen, W.N. Kang, Eun-Mi Choi, Hyeong-Jin Kim, and Sung-Ik Lee, *Phys. Rev. Lett.* **87**, 277001 (2001).
- ²⁰ A.B. Kuzmenko, F.P. Mena, H.J.A. Molegraaf, D. van der Marel, B. Gorshunov, M. Dressel, I.I. Mazin, J. Kortus, O.V. Dolgov, T. Muranaka, and J. Akimitsu, *Solid State Commun.* **121**, 479 (2002).
- ²¹ I.I. Mazin, O.K. Andersen, O. Jepsen, O.V. Dolgov, J. Kortus, A.A. Golubov, A.B. Kuzmenko, and D. van der Marel, *Phys. Rev. Lett.* **89**, 107002 (2002).
- ²² Mi-Ock Mun, Young Jin Kim, Yu Park, Jae Hoon Kim, S.H. Moon, H.N. Lee, H.G. Kim, and B. Oh, *J. of Supercond.* **15**, 475 (2002).
- ²³ Y. Fudamoto and S. Lee, *Phys. Rev. B* **68**, 184514 (2003).
- ²⁴ F. Marsiglio, *Phys. Rev. Lett.* **87**, 247001 (2001).
- ²⁵ E.G. Maksimov, J. Kortus, O.V. Dolgov, and I. I. Mazin, *Phys. Rev. Lett.* **89**, 129703 (2002).
- ²⁶ D. Chvostova, V. Zelezny, L. Pajasova, A. Tarasenko, A. Plecenik, P. Kus, and L. Satrapinsky, *Thin Solid Films* **455**, 213 (2004).
- ²⁷ J. Karpinski, M. Angst, J. Jun, S. M. Kazakov, R. Puzniak, A. Wisniewski, J. Roos, H. Keller, A. Perucchi, L. Degiorgi, M. R. Eskildsen, P. Bordet, L. Vinnikov and A. Mironov, *Supercond. Sci. Technol.* **16**, 221 (2002).
- ²⁸ A.B.Kuzmenko, *Rev. Sci. Instrum.* **76**, 083108 (2005).
- ²⁹ O.V.Dolgov and S.V. Shulga, *J. Supercond.* **8**, 511 (1995).
- ³⁰ V.P. Antropov, K.D. Belashchenko, M. van Schilfgaarde, and S.N. Rashkeev, *cond-mat/0107123*.
- ³¹ P. Ravindran, P. Vajeeston, R. Vidya, A. Kjekshus, and H. Fjellvag, *Phys. Rev. B* **64** 224509 (2001).
- ³² J. Kortus, I.I. Mazin, K.D. Belashchenko, V.P. Antropov, and L.L. Boyer, *Phys. Rev. Lett.* **86**,4656 (2001).
- ³³ W. Ku, W.E. Pickett, R.T. Scalettar, and A.G. Eguluz, *Phys. Rev. Lett.* **88**, 057001 (2002).
- ³⁴ O.V.Dolgov, Y. Kong, J. Kortus and O. Jepsen, private communication.
- ³⁵ H. Rosner, J.M. An, W.E. Pickett, and S.-L. Drechsler, *Phys. Rev. B* **66**, 024521 (2002).
- ³⁶ I.I. Mazin and J. Kortus, *Phys. Rev. B*, **65** 180510(R) (2002).
- ³⁷ A.V. Sologubenko, J. Jun, S.M. Kazakov, J. Karpinski, and H.R. Ott, *Phys. Rev. B* **66**, 014504 (2002).
- ³⁸ J.W. Quilty, S. Lee, S. Tajima, and A. Yamanaka, *Phys. Rev. Lett.* **90**, 207006 (2003).
- ³⁹ S. Lee, *Physica C* **385** 31 (2003).
- ⁴⁰ P.E. Sulewski, T.W. Noh, J.T. McWhirter, and A.J. Sievers, *Phys. Rev. B* **36**, R5735 (1987).
- ⁴¹ D.E. Aspnes, *J. Opt. Soc. Am.* **70**, 1275 (1980).